NUCL SCI TECH (2017) 28:155
DOI 10.1007/s41365-017-0320-x

Energy calibration of laterally segmented electromagnetic calorimeters based on neutral pion detection

Malek Mazouz[1]

Received: 8 March 2017 / Revised: 10 June 2017 / Accepted: 11 June 2017 / Published online: 25 October 2017

Abstract This paper describes a method for energy calibration of laterally segmented electromagnetic calorimeters based on the detection of two-photon decays of π^0 mesons. The calibration procedure performs a χ^2 function minimization between the measured π^0 energy in the calorimeter and its expected energy deduced from the π^0 momentum direction. The performance of this technique is demonstrated with a Monte Carlo simulation of an experimental case where biased calibration coefficients are employed. The real calibration coefficients are restored with less than 1% relative accuracy when a sufficient number of π^0 is detected. This technique is applied to monitor daily the calibration coefficients of the calorimeter used in the Jefferson Lab Hall A DVCS experiments.

Keywords Electromagnetic calorimeters · Energy calibration · Detector modeling and simulations · Data processing methods

1 Introduction

The main goal of electromagnetic calorimeters is to measure precisely the energy of detected particles such as photons and electrons. These detectors are important elements in nuclear physics instrumentation and are widely used especially in hadronic and particle physics experiments [1]. Usually, the knowledge of the impact position of detected particles is required leading to a lateral segmentation of these calorimeters. Lead fluoride (PbF_2) is commonly employed as a constituent material of such calorimeters [2–5]. Its high density offers a short radiation length ($X_0 = 0.93$ cm) and a small Molière radius ($r_M = 2.12$ cm) leading to compact detector geometries [6, 7]. In practice, the segmentation size is close to r_M, while the longitudinal calorimeter length is equal to several X_0 to ensure a full development of electromagnetic showers in the detector blocks. Each calorimeter block is generally connected to a photomultiplier tube (PMT) to collect the light induced by a shower and an electronic base to shape and amplify the PMT signal. The amplitude of the final signal is then related to the energy released by the particle in the considered block via a calibration coefficient.

A great deal of effort is still underway to optimize the performance of electromagnetic calorimeters and, in particular, their energy resolution [8–10]. In addition to the design optimization, many energy calibration techniques are still investigated to improve the reconstructed energy of detected particles [11–14]. Indeed, the energy calibration is sensitive to many factors, such as the hadronic and electromagnetic background during the experiment and the gain drift of blocks due to an increasing loss of their transparency when exposed to high radiation rates and accumulated doses [15, 16]. The choice of the energy calibration method is then crucial to ensure a frequent and proper monitoring of the calibration coefficients of each calorimeter block keeping thus an acceptable energy resolution. In many experiments, dedicated calibration runs have to be taken in order to send particles of known energy in the calorimeter. Other methods consist to calibrate the detector with cosmic rays or with a cluster of LEDs of known light intensity placed in front of the calorimeter

✉ Malek Mazouz
mazouz@jlab.org

[1] Faculté des Sciences de Monastir, 5000 Monastir, Tunisia

blocks [16]. All these standard methods have the disadvantage to change momentarily the experimental setting or trigger and to decrease the amount of time dedicated to physics runs. In addition, many parameters, such as the nature of particles used in the calibration procedure, their energies and incident angles, and the experimental background, could be different relative to the physics run conditions. The obtained calibration coefficients are then not necessarily optimized for the particles detected during physics runs. Finally, the calibration provided by these methods at a given time may not still be valid afterward if the calibration coefficients are time dependent.

This paper presents an energy calibration method based on the detection of π^0 mesons in the calorimeter. This method is performed to monitor daily the calibration of the electromagnetic calorimeter of the Jefferson Lab Hall A DVCS experiments [2, 3, 17, 18] and can be applied in similar experiments where two-photon decays of π^0 can be detected in a laterally segmented calorimeter. It does not require specific runs since the calibration data are taken simultaneously with the primary experimental data at the same conditions. This method will be exposed and tested on the basis of a calorimeter simulation using the GEANT4 toolkit [19]. The relative accuracy on the obtained calibration coefficients will finally be discussed in terms of the number of detected π^0.

2 Simulation of an experimental case

The main goal of the Jefferson Lab Hall A DVCS experiments is to study the deeply virtual Compton scattering (DVCS) process on the nucleon $eN \rightarrow eN\gamma$ using a few GeV electron beams impinging on a liquid hydrogen (LH2) or deuterium (LD2) target [2, 3, 17, 18]. Many similar experiments in the world are concerned with this increasingly timely topic of the characterization of the nucleon structure with the DVCS process [20–23]. As shown in Fig. 1, the scattered electron is detected in a high-resolution spectrometer (HRS) which determines accurately its momentum and angles as well as the reaction vertex coordinates in the target [24]. The emitted photon is detected in an electromagnetic calorimeter consisting of a 16×13 matrix of $3 \times 3 \times 18.6$ cm^3 PbF_2 blocks placed at 1.1 m from the target. This short distance combined with the high luminosity of the experiment ($\sim 10^{37}$ cm^{-2}s^{-1}) leads to an important background rate in the calorimeter as well as radiation damage near the front face of blocks. The energy calibration of the calorimeter is of direct relevance since it affects directly the $eN \rightarrow eN\gamma$ event identification based on a study of the missing mass squared:

$$M_x^2 = \left(k + p - k' - q'_\gamma\right)^2, \tag{1}$$

where k, k', p and q'_γ are, respectively, the 4-vectors of the incident electron, the scattered electron, the initial nucleon at rest and the emitted photon. Experimentally, k, k' and p are known accurately and the resolution of M_x^2 is dominated by the calorimeter energy resolution [16]. The photon 4-vector is determined for each event, j, from the energies deposited in the calorimeter blocks:

$$E'_i(j) = C'_i A_i(j), \tag{2}$$

where $A_i(j)$ is the output signal amplitude of block i and C'_i is the corresponding calibration coefficient. Let us assume that the C'_i coefficients are roughly known at a given time with any standard calibration method. As mentioned above, many factors, such as different experimental conditions and transparency losses of blocks, could modify the calibration by 20% in average [25] and by up to 40% for some particular blocks:

$$C_i = \epsilon_i C'_i. \tag{3}$$

The correction factors, ϵ_i, and thus the new calibration coefficients, C_i, must then be known accurately in order to get the real deposited energies, $E_i(j)$:

$$E_i(j) = \epsilon_i C'_i A_i(j) = \epsilon_i E'_i(j). \tag{4}$$

The goal of the calibration method, discussed hereafter, is to determine the ϵ_i for each block, i. This method is based on the study of π^0 electroproduction events $eN \rightarrow eN\pi^0 \rightarrow eN\gamma\gamma$ where the two photons coming from the π^0 decay are detected in the calorimeter. This reaction is very common in lepton–hadron scattering and is usually present in the data of DVCS experiments. The π^0 energy is almost equal to the DVCS photon energy because of the kinematic similarity between these two reactions, and it is then well adapted for the calorimeter calibration.

To demonstrate the validity of the calibration method, a GEANT4 simulation of the experimental setup is performed and $N = 2.10^6$ $eN \rightarrow eN\pi^0$ events are generated following the kinematics presented in Table 1. This particular kinematics corresponds to one setting of the Hall A DVCS experiments [26]. The electromagnetic showers created by the π^0 photons in the calorimeter are fully simulated [27]. The generation and tracking of Čerenkov photons induced by the showers in the PbF_2 blocks are not considered in this study because of unrealistic computing times and strong sensitivity to exact optical properties of crystals and their wrapping surfaces. However, one can attribute an average number of $N_{\mathrm{ph}} = 330$ photoelectrons per GeV deposit collected by the PMT of each block to be coherent with the reported experimental energy resolution

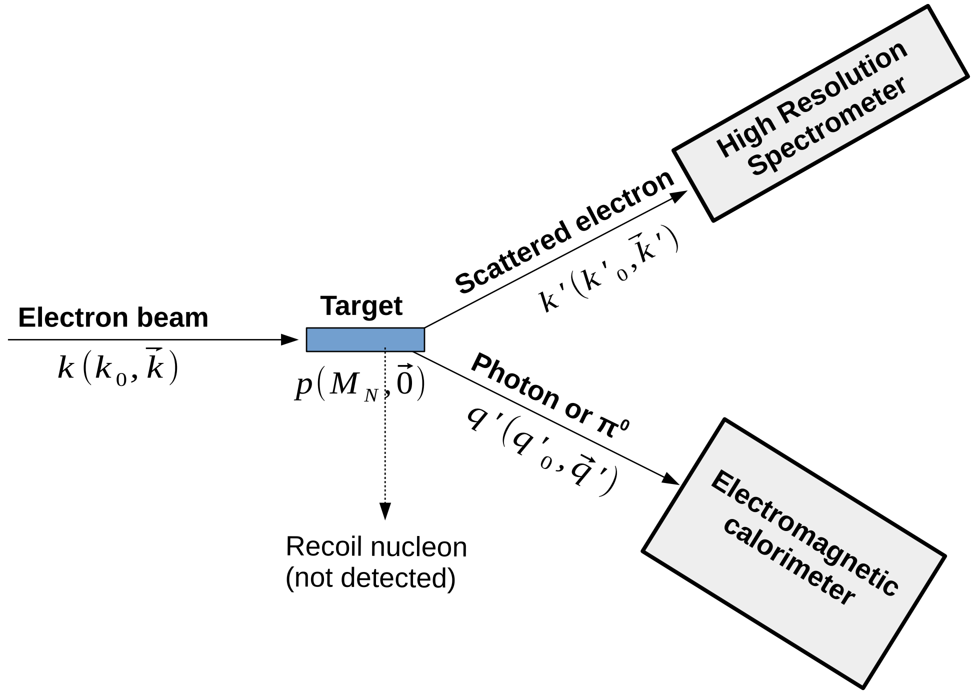

Fig. 1 Experimental setup of the Hall A DVCS experiments and definition of particle 4-vectors. $q' = q'_\gamma$ ($q' = q'_2 + q'_1$) is the photon (π^0) 4-vector. The recoil nucleon, not detected, is identified with a cut on the missing mass squared defined by Eq. (1) (Eq. 12) if a photon (π^0) is detected in the calorimeter

Table 1 Simulated kinematics. $\theta_{kk'}$ ($\theta_{kq'}$) is the polar angle between the scattered electron (π^0) and the incident electron. $\phi_{kq'}$ is the azimuthal angle of the π^0 relative to the incident electron. $<q'_0>$ is the mean π^0 energy within the calorimeter acceptance

k_0 (GeV)	k'_0 (GeV)	$\theta_{kk'}$ (°)	$<q'_0>$ (GeV)	$\theta_{kq'}$ (°)	$\phi_{kq'}$ (°)
4.455	[1.78, 1.96]	[25, 28]	2.4	[9, 28]	[– 50, 50]

$\sigma(E)/E = 3.1\%$ [26]. This number is deduced from a $H(e, e'_{\text{Calo}} p_{\text{HRS}})$ elastic calibration where $E'_e = 3.16$ GeV scattered electrons are detected in the calorimeter:

$$3.1\% = \frac{\sigma(E'_e)}{E'_e} = \frac{1}{\sqrt{N_{\text{ph}}\, E'_e(\text{GeV})}}. \tag{5}$$

Finally, real radiative effects, where the incident or the scattered electron emits a real photon, are taken into account in the simulation following the procedure described in Ref. [16].

To mimic the uncertainty on the experimental calibration coefficients, the energies, E_i, deposited in the calorimeter blocks are multiplied by random numbers, K_i, varying uniformly between $1 - K_{\max}$ and 1, where $K_{\max} = 40\%$, and become equal to:

$$E'_i(j) = K_i E_i(j). \tag{6}$$

The calibration method consists then to determine, from $E'_i(j)$ and the known 4-vectors $\{k,\, k'(j),\, p\}$, the correction factors, ϵ_i, which have to be applied in order to get the correct energies. It is evident from Eqs. (4) and (6) that a successful calibration should give $\epsilon_i \approx 1/K_i$ with $\delta_i = \epsilon_i K_i - 1$ being the relative deviation of ϵ_i from $1/K_i$.

3 Calibration method

The calibration method is based on a χ^2 minimization between the measured π^0 energy, $E^{\text{rec}}_{\pi^0}$, reconstructed from E'_i, and the expected π^0 energy, $E^{\text{cal}}_{\pi^0}$, calculated from the π^0 momentum direction. The following subsections detail the different steps of the calibration.

3.1 Particle 4-vector reconstruction

The reconstructed π^0 energy in the simulation is the sum of the two shower energies created by the two photons of the π^0 decay. Experimentally, one can have multiple showers in the calorimeter coming from other meson decays, accidentals or any additional final state particles. In this case, a clustering algorithm based on a cellular automata is used to determine the number of showers and to separate the different cluster contributions [28]. The energy of a shower is then the sum of the energies deposited in the N_{clus} blocks belonging to the corresponding cluster:

$$E'_{\text{sh}} = \sum_i^{N_{\text{clus}}} E'_i. \tag{7}$$

Figure 2 shows an example of a π^0 event in the calorimeter where the corresponding clusters are indicated

Fig. 2 (Color online) Numbering of the calorimeter blocks. The blocks located at the calorimeter edge are shown in blue. An example of a two-cluster event created by the $\pi^0 \to \gamma\gamma$ decay is shown with the red blocks

16	32	48	64	80	96	112	128	144	160	176	192	208
15	31	47	63	79	95	111	127	143	159	175	191	207
14	30	46	62	78	94	110	126	142	158	174	190	206
13	29	45	61	77	93	109	125	141	157	173	189	205
12	28	44	60	76	92	108	124	140	156	172	188	204
11	27	43	59	75	91	107	123	139	155	171	187	203
10	26	42	58	74	90	106	122	138	154	170	186	202
9	25	41	57	73	89	105	121	137	153	169	185	201
8	24	40	56	72	88	104	120	136	152	168	184	200
7	23	39	55	71	87	103	119	135	151	167	183	199
6	22	38	54	70	86	102	118	134	150	166	182	198
5	21	37	53	69	85	101	117	133	149	165	181	197
4	20	36	52	68	84	100	116	132	148	164	180	196
3	19	35	51	67	83	99	115	131	147	163	179	195
2	18	34	50	66	82	98	114	130	146	162	178	194
1	17	33	49	65	81	97	113	129	145	161	177	193

in red. The transverse coordinates (x_c, y_c) of a shower centroid are determined with a center of gravity-based method from the coordinates (x_i, y_i) of the blocks belonging to the corresponding cluster [29]:

$$x_c = \frac{\sum_i w_i x_i}{\sum_i w_i}, \tag{8}$$

with a similar equation for y_c. The weight, w_i, is given by:

$$w_i = \max\left\{0; W_0 + \ln\left(\frac{E'_i}{E'_{\text{sh}}}\right)\right\}, \tag{9}$$

where W_0 is a free dimensionless parameter optimized for the considered energies [30]. The showers whose centroid coordinates belong to a block of the calorimeter edge (see Fig. 2) are excluded from the calibration procedure. Indeed, the energy of a particle impinging these particular blocks is not well reconstructed because of the shower energy leakage near the calorimeter edge.

The knowledge of the shower centroid coordinates, with a 3 mm accuracy [26], and the interaction vertex coordinates allows us to reconstruct the momentum direction of the particle creating the shower and thus its 4-vector $q'(E'_{\text{sh}}, \vec{q}\,')$, assuming a photon as a detected particle. The different steps of this reconstruction procedure are applied for each simulated event to be coherent with the experimental data analysis. It is worth noting that the obtained particle direction is not very sensitive to the deposited energies, E'_i, and thus to the calibration coefficients, but depends mainly on the block coordinates where a maximum energy is released by the shower [30]. Consequently, the angle between the particle direction and the virtual photon momentum, $\vec{q} = \vec{k} - \vec{k}'$, is well reconstructed even if inadequate calibration coefficients are employed.

3.2 $eN \to eN\pi^0$ reaction identification

In the simulated data, only $eN \to eN\pi^0 \to eN\gamma\gamma$ events are generated. Experimentally, we have to identify this reaction by selecting only two-cluster events and by computing the invariant mass of the two reconstructed particles in the calorimeter:

$$M_{\text{inv}} = \sqrt{\left(q'_1 + q'_2\right)^2}, \tag{10}$$

where q'_1 and q'_2 are the particle 4-vectors determined as described in the previous subsection. If these particles are photons coming from a π^0 decay, then their invariant mass should be equal to the π^0 mass $M_{\pi^0} \approx 0.135$ GeV, within detector resolution. In an experimental or simulated M_{inv} distribution, π^0 events are located in a peak around M_{π^0} and cannot be confused with other mesons or events. However, a miscalibration of the calorimeter blocks can shift the peak position (M_{peak}) and increase its width ($\sigma_{M_{\text{inv}}}$) as shown in the simulated M_{inv} histogram of Fig. 3. A cut around the peak position, instead of M_{π^0}, is then applied to ensure the selection of π^0 events:

$$|M_{\text{inv}} - M_{\text{peak}}| < 3\,\sigma_{M_{\text{inv}}}, \tag{11}$$

where $\sigma_{M_{\text{inv}}}$ is the resolution of the reconstructed M_{inv} variable.

The second step of the $eN \to eN\pi^0$ reaction identification consists to compute for each π^0 event the missing mass squared defined by:

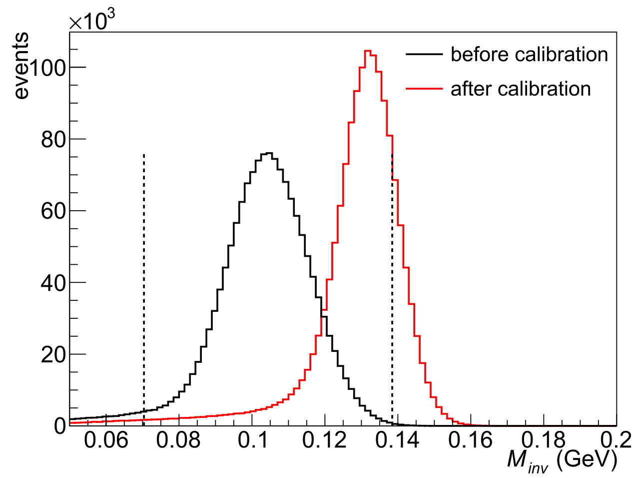

Fig. 3 (Color online) Simulated two-gamma invariant mass distribution before (black) and after (red) the calibration. The vertical dashed lines represent the M_{inv} cut of Eq. (11)

$$M_x^2 = \left(k + p - k' - q_1' - q_2'\right)^2, \tag{12}$$

which must be equal to the nucleon mass squared $M_N^2 \approx 0.88\ \mathrm{GeV}^2$ within detector resolution if the considered event corresponds to a $eN \rightarrow eN\pi^0$ reaction and if the calorimeter is well calibrated. Figure 4 shows the simulated M_x^2 distribution where only $eN \rightarrow eN\pi^0$ events are generated. The peak position in Fig. 4 is not centered around M_N^2 because of the E_i smearing by the random factors, K_i, which is equivalent experimentally to a wrong calibration of the blocks. The non-Gaussian behavior of the right side of the peak is due to real radiative effects. Experimentally, deep inelastic scattering (DIS) events, where additional mesons are created in the final state, are also present in a M_x^2 distribution and are located after the

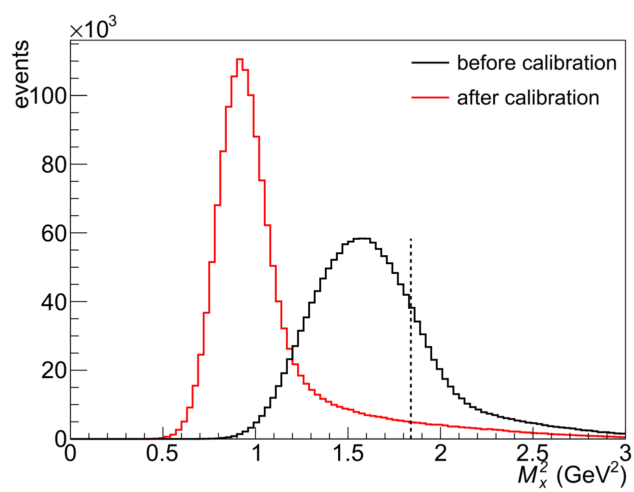

Fig. 4 (Color online) Simulated missing mass squared distribution before (black) and after (red) the calibration. The vertical dashed line represents the M_x^2 cut of Eq. (13)

M_x^2 peak position (see Fig. 2 in Ref. [26] for more details). To avoid the contamination from DIS events, the selection of $eN \rightarrow eN\pi^0$ is performed, as shown in Fig. 4, by applying the following M_x^2 cut:

$$M_x^2 < M_{\mathrm{peak}}^2 + \sigma_{M_x^2}, \tag{13}$$

where M_{peak}^2 is the peak position in the M_x^2 distribution and $\sigma_{M_x^2}$ its resolution. Both Eqs. (11) and (13) cuts are applied in the simulation to be coherent with the experimental data analysis.

3.3 Expected π^0 energy calculation

For each selected $eN \rightarrow eN\pi^0$ event, the reconstructed π^0 energy writes:

$$E_{\pi^0}^{\mathrm{rec}} = \sum_{i=1}^{208=16\times 13} E_i' d_i, \tag{14}$$

where $d_i = 1$ if the block, i, belongs to one of the two clusters created by the π^0 and $d_i = 0$ otherwise. This reconstructed energy leads to particular values of M_x^2 and M_{inv} which can be different from M_N^2 and M_{π^0} because of energy resolution effects or a bad calibration of blocks. Actually, it is possible to find for each event a more realistic estimation of the pion energy, called $E_{\pi^0}^{\mathrm{cal}}$ hereafter, giving exactly $M_x^2 = M_N^2$ and $M_{\mathrm{inv}} = M_{\pi^0}$. Equations (10) and (12) lead to:

$$\begin{aligned} M_N^2 &= \left(k + p - k' - q_1' - q_2'\right)^2 \\ &= (k + p - k')^2 + M_{\pi^0}^2 \\ &\quad - 2(k_0 - k_0' + M_N)E_{\pi^0}^{\mathrm{cal}} + 2\|\vec{q}\|\sqrt{\left(E_{\pi^0}^{\mathrm{cal}}\right)^2 - M_{\pi^0}^2}\cos\theta, \end{aligned} \tag{15}$$

where θ is the angle between the momenta of the virtual photon and the π^0. As mentioned above, θ is well defined experimentally even if biased calibration coefficients are employed. The physical solution of Eq. (15) is given by:

$$E_{\pi^0}^{\mathrm{cal}} = \frac{-b + \sqrt{b^2 - 4ac}}{2a}, \tag{16}$$

where

$$\begin{aligned} a &= 4\left(k_0 - k_0' + M_N\right)^2 - 4\|\vec{q}\|^2\cos^2\theta, \\ b &= 4\left(k_0 - k_0' + M_N\right)\left[M_N^2 - (k - k' + p)^2 - M_{\pi^0}^2\right], \\ c &= 4M_{\pi^0}^2\|\vec{q}\|^2\cos^2\theta + \left[M_N^2 - (k - k' + p)^2 - M_{\pi^0}^2\right]^2. \end{aligned} \tag{17}$$

Figure 5 shows the histogram of the relative difference between $E_{\pi^0}^{\mathrm{cal}}$ and the real π^0 energy, $E_{\pi^0}^{\mathrm{real}}$, known for each

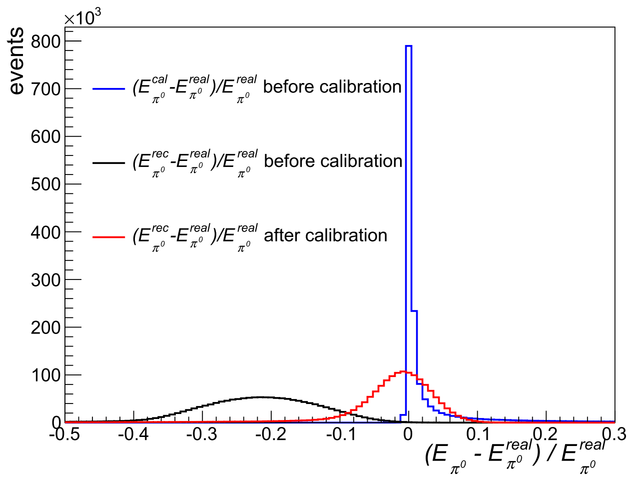

Fig. 5 (Color online) Relative difference between the real π^0 energy, $E_{\pi^0}^{\text{real}}$, and the reconstructed π^0 energy, $E_{\pi^0}^{\text{rec}}$, before (black) and after (red) the calibration. The relative difference between, $E_{\pi^0}^{\text{real}}$, and the calculated π^0 energy, $E_{\pi^0}^{\text{cal}}$, (Eq. (16)) is shown with the blue histogram

event in the simulation. The comparison between the reconstructed π^0 energy, $E_{\pi^0}^{\text{rec}}$, and $E_{\pi^0}^{\text{real}}$ is also shown in Fig. 5. The mean value and the small RMS of the $(E_{\pi^0}^{\text{cal}} - E_{\pi^0}^{\text{real}})$ distribution relative to the $(E_{\pi^0}^{\text{rec}} - E_{\pi^0}^{\text{real}})$ distribution indicate that $E_{\pi^0}^{\text{cal}}$ is much closer to the real π^0 energy than $E_{\pi^0}^{\text{rec}}$. The calculated π^0 energy can then be used to adjust the calorimeter calibration and determine the correction factors ϵ_i as detailed in the following subsection.

3.4 χ^2 minimization

For each $eN \to eN\pi^0$ event, j, $E_{\pi^0}^{\text{cal}}(j)$ gives a realistic estimation of the π^0 energy and thus of what the energy deposited in the calorimeter should be. The correction factors, ϵ_i, are then those minimizing the χ^2 defined by:

$$\chi^2 = \sum_{j=1}^{N_{\pi 0}} \left(E_{\pi^0}^{\text{cal}}(j) - E_{\pi^0}^{\text{rec}}(j)\right)^2, \tag{18}$$

where N_{π^0} is the total number of events and $E_{\pi^0}^{\text{rec}}(j)$ is the reconstructed π^0 energy determined with the correction factors ϵ_i:

$$E_{\pi^0}^{\text{rec}}(j) = \sum_{i=1}^{208} \epsilon_i E_i'(j) d_i(j). \tag{19}$$

The minimization of Eq. (18) writes:

$$\frac{d\chi^2}{d\epsilon_k} = -2\sum_{j=1}^{N_{\pi 0}} \left[E_{\pi^0}^{\text{cal}}(j) - \sum_{i=1}^{208} \epsilon_i E_i'(j) d_i(j)\right] E_k'(j) d_k(j) = 0 \quad \forall k = 1, 2, \ldots, 208 \tag{20}$$

and yields to the following linear set of equations:

$$\sum_{i=1}^{208} \left[\sum_{j=1}^{N_{\pi 0}} E_i'(j) d_i(j) E_k'(j) d_k(j)\right] \epsilon_i = \sum_{j=1}^{N_{\pi 0}} E_{\pi^0}^{\text{cal}}(j) E_k'(j) d_k(j) \quad \forall k = 1, 2, \ldots, 208 \tag{21}$$

The correction factors, ϵ_i, are then obtained by inverting the 208×208 matrix, $\alpha_{ik} = \sum_{j=1}^{N_{\pi^0}} E_i'(j) d_i(j) E_k'(j) d_k(j)$. Experimentally, this minimization procedure provides the adjusted calibration coefficients defined by Eq. (3).

4 Results and discussion

Figure 6 shows the relative difference $\delta_i = \epsilon_i K_i - 1$ between the obtained correction factors, ϵ_i, and the smearing factors, $1/K_i$, as a function of the calorimeter block number. Figure 6 proves that the present calibration method succeeds to find the real calibration coefficients for all the calorimeter blocks, within 1% deviation, except for those located at the calorimeter edge. Since the clusters centered around the latter blocks are excluded from the calibration procedure, the α-matrix diagonal elements corresponding to these blocks are filled with low deposited energies and become sensitive to energy fluctuations of shower tails. The corresponding calibration coefficients are then slightly overestimated. The energy resolution improvement is shown in Fig. 5 where a clear decrease in the $(E_{\pi^0}^{\text{rec}} - E_{\pi^0}^{\text{real}})$ distribution RMS is visible after this calibration. The calibration quality is also shown in Figs. 3 and 4 where the peaks corresponding, respectively, to π^0 events and $eN \to eN\pi^0$ events are now centered around M_{π^0} and M_N^2 with a smaller width.

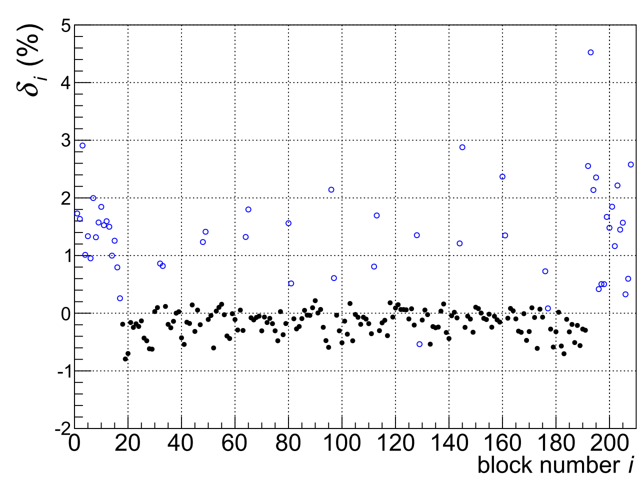

Fig. 6 (Color online) Relative difference, δ_i, between the correction factors, ϵ_i, and the smearing factors, $1/K_i$, as a function of the calorimeter block number, i. The blocks located at the calorimeter edge (see Fig. 2) are represented with blue open circles

The average relative accuracy on the obtained correction factors or calibration coefficients can be defined as:

$$\Delta = \sqrt{\frac{1}{154}\sum_i \delta_i^2}, \tag{22}$$

where the sum runs over the block numbers not belonging to the calorimeter edge. This relative accuracy decreases when the number, N_π^0, of $eN \to eN\pi^0$ events, used in the calibration procedure, increases. For other segmented calorimeters composed of N_b blocks, Δ should rather depend of N_{π^0}/N_b assuming a uniform π^0 distribution in the calorimeter acceptance. Figure 7 shows the evolution of Δ as a function of N_{π^0}/N_b and demonstrates that less than 1% average accuracy on the calibration coefficients can be obtained if N_{π^0}/N_b is larger than 100. A fit of Fig. 7 points leads to the following empirical power law:

$$\Delta(\%) = 5.22\,(N_{\pi^0}/N_b)^{-0.386}. \tag{23}$$

The number N_{π^0}/N_b depends experimentally on the integrated luminosity and the differential cross section of the $eN \to eN\pi^0$ process in the studied kinematics. For example, the average π^0 production rate for the kinematics of Table 1 is $N_{\pi^0}/N_b \approx 90$ per day. A compromise on the calibration frequency during the experiment should then be found taking into account the drift rate of the block gains. For the Jefferson Lab Hall A DVCS experiments, a daily monitoring of the calorimeter calibration coefficients is achieved at 1% accuracy level with this calibration method [26].

In some extreme cases when some initial calibration coefficients are different from the real ones by a considerable amount, iterations of the different steps discussed in Sect. 3 could be necessary. This is mainly due experimentally to an identification issue of the $eN \to eN\pi^0$ events because of a possible contamination of the selected yield (Eq. 13) by DIS events. A more selective M_x^2 cut can then be applied in the first iteration to minimize this contamination. The calibration coefficients obtained after the first iteration are used as initial calibration coefficients for the second iteration and so on. A convergence of the calibration coefficients is generally obtained after the second or the third iteration.

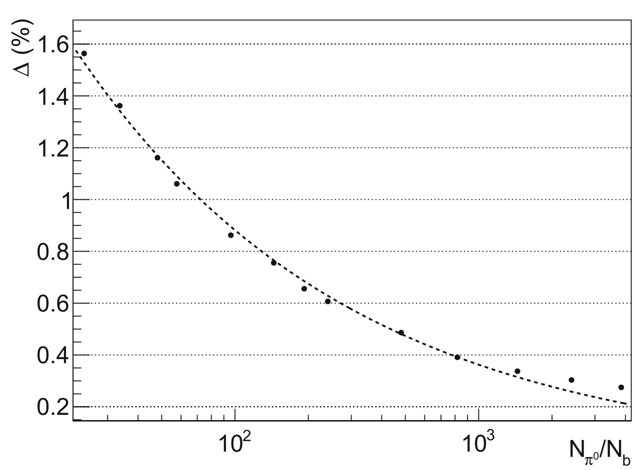

Fig. 7 Average relative accuracy, Δ, on the calibration coefficients as a function of the ratio between the number of π^0 used in the calibration procedure and the number of calorimeter blocks ($N_b = 208$). The dashed line represents Eq. (23) fit to the points

5 Conclusion

The present work discussed an energy calibration technique of laterally segmented electromagnetic calorimeters where the two photons of the π^0 decay produced by the $eN \to eN\pi^0$ reaction are detected. The calibration procedure is based on a χ^2 minimization between the reconstructed π^0 energy, from the calorimeter block data, and its expected energy. This energy is calculated for each event from the π^0 momentum direction, exploiting the good spatial resolution of the calorimeter. Contrary to other standard calibration methods, this technique allows us to have a set of calibration coefficients optimized for the studied particles under real experimental conditions. The average relative accuracy on these coefficients is less than 1% if the number of detected π^0 events relative to the number of calorimeter blocks is larger than 100. This technique has been successfully applied to monitor daily the calorimeter calibration of the Jefferson Lab Hall A DVCS experiments at a 1% accuracy level and with a continuous loss of block transparencies. The calibration method can be applied similarly using any other exclusive meson electroproduction reaction if all-photon decays of these mesons are detected in the calorimeter.

References

1. R.-Y., Zhu et al., in *Proceedings of the Tenth International Conference on Calorimetry in Particle Physics*, Pasadena, California, USA, 25–29 March 2002
2. C.M. Camacho, A. Camsonne, M. Mazouz et al. (Jefferson Lab Hall A Collaboration), Scaling tests of the cross-section for deeply virtual compton scattering. Phys. Rev. Lett. **97**, 262002 (2006). doi:10.1103/PhysRevLett.97.262002
3. M. Mazouz, A. Camsonne, C.M. Camacho et al. (Jefferson Lab Hall A Collaboration), Deeply virtual compton scattering off the neutron. Phys. Rev. Lett. **99**, 242501 (2007). doi:10.1103/PhysRevLett.99.242501
4. F.E. Maas et al. (A4 Collaboration), Measurement of strange quark contributions to the nucleon's form-factors at $Q^2 = 0.230$ (GeV/c)^2. Phys. Rev. Lett. **93**, 022002 (2004). doi:10.1103/PhysRevLett.93.022002

5. J. Grange et al., Muon (g-2) Technical Design Report, FERMI-LAB-FN-0992-E. (2015). doi:10.2172/1251172
6. D.F. Anderson, M. Kobayashi, Y. Yoshimura, C.L. Woody, Lead fluoride: an ultracompact Cherenkov radiator for EM calorimetry. Nucl. Instrum. Meth. A **290**, 385 (1990). doi:10.1016/0168-9002(90)90553-I
7. K.A. Olive et al., Review of Particle Physics. Chin. Phys. C **38**, 090001 (2014). doi:10.1088/1674-1137/38/9/090001
8. A.T. Fienberg et al., Studies of an array of PbF_2 Cherenkov crystals with large-area SiPM readout. Nucl. Instrum. Meth. A **783**, 12 (2015). doi:10.1016/j.nima.2015.02.028
9. I. Balossino et al., The HPS electromagnetic calorimeter. Nucl. Instrum. Meth. A **854**, 89 (2017). doi:10.1016/j.nima.2017.02.065
10. C. Zhang, FoCal—a high granularity electromagnetic calorimeter for forward direct photon measurements. Nucl. Instrum. Meth. A **845**, 542 (2017). doi:10.1016/j.nima.2016.06.075
11. S. Baunack et al., Real-time calibration of the A4 electromagnetic lead fluoride (PbF_2) calorimeter. Nucl. Instrum. Meth. A **640**, 58 (2011). doi:10.1016/j.nima.2011.02.099
12. Y.-F. Xu, J.-H. Chen et al., Physics performance of the STAR zero degree calorimeter at relativistic heavy ion collider. Nucl. Sci. Tech. **27**, 126 (2016). doi:10.1007/s41365-016-0129-z
13. R.T. Jones, M. Kornicer et al., A bootstrap method for gain calibration and resolution determination of a lead-glass calorimeter. Nucl. Instrum. Meth. A **566**, 366 (2006). doi:10.1016/j.nima.2006.07.061
14. M. Mazouz., E. Voutier, Monitoring of the calibration constants of the DVCS calorimeter, JLAB-TN-05-033 (2005)
15. P. Kozma, R. Bajgarb, P. Kozma Jr., Radiation resistivity of PbF2 crystals. Nucl. Instrum. Meth. A **484**, 149 (2002). doi:10.1016/S0168-9002(01)02011-3
16. M. Defurne et al. (Jefferson Lab Hall A Collaboration), E00–110 experiment at Jefferson Lab Hall A: deeply virtual Compton scattering off the proton at 6 GeV. Phys. Rev. C **92**, 055202 (2015). doi:10.1103/PhysRevC.92.055202
17. C. Munoz Camacho, P. Bertin, C.E. Hyde, J. Roche, et al. (Hall A DVCS Collaboration), Separation of deeply virtual photon and π^0 electroproduction observables of unpolarized protons, JLab experiment E07-007 (2007)
18. M. Mazouz, A. Camsonne, C.E. Hyde et al. (Hall A DVCS Collaboration), Measurement of the deeply virtual Compton scattering off the neutron, JLab Experiment E08-025 (2008)
19. S. Agostinelli et al. (GEANT4 Collaboration), GEANT4: a simulation toolkit. Nucl. Instrum. Meth. A **506**, 250 (2003). doi:10.1016/S0168-9002(03)01368-8
20. F.-X. Girod et al. (CLAS Collaboration), Measurement of deeply virtual Compton scattering beam-spin asymmetries. Phys. Rev. Lett. **100**, 162002 (2008). doi:10.1103/PhysRevLett.100.162002
21. S. Chekanov et al. (ZEUS Collaboration), Measurement of deeply virtual Compton scattering at HERA. Phys. Lett. B **573**, 46 (2003). doi:10.1016/j.physletb.2003.08.048
22. F.D. Aaron et al. (H1 Collaboration), Measurement of deeply virtual Compton scattering and its t-dependence at HERA. Phys. Lett. B **659**, 796 (2008). doi:10.1016/j.physletb.2007.11.093
23. A. Airapetian et al. (HERMES Collaboration), Beam-helicity asymmetry arising from deeply virtual Compton scattering measured with kinematically complete event reconstruction. J. High Energ. Phys. **10**, 042 (2012). doi:10.1007/JHEP10(2012)042
24. J. Alcorn et al., Basic instrumentation for Hall A at Jefferson Lab. Nucl. Instrum. Meth. A **522**, 294 (2004). doi:10.1016/j.nima.2003.11.415
25. E. Fuchey, A. Camsonne, C. Munoz, M. Mazouz et al. (Jefferson Lab Hall A Collaboration), Exclusive neutral pion electroproduction in the deeply virtual regime. Phys. Rev. C **83**, 025201 (2011). doi:10.1103/PhysRevC.83.025201
26. M. Defurne, M. Mazouz et al. (Jefferson Lab Hall A Collaboration), Rosenbluth separation of the π^0 electroproduction cross section. Phys. Rev. Lett. **117**, 262001 (2016). doi:10.1103/PhysRevLett.117.262001
27. G. Grindhammer, M. Rudowicz, S. Peters, The fast simulation of electromagnetic and hadronic showers. Nucl. Instrum. Meth. A **290**, 469 (1990). doi:10.1016/0168-9002(90)90566-O
28. V. Breton et al., Application of neural networks and cellular automata to interpretation of calorimeter data. Nucl. Instrum. Meth. A **362**, 478 (1995). doi:10.1016/0168-9002(95)00217-0
29. T.C. Awes, F.E. Obenshain, F. Plasil, S. Saini, S.P. Sorensen et al., A simple method of shower localization and identification in laterally segmented calorimeters. Nucl. Instrum. Meth. A **311**, 130 (1992). doi:10.1016/0168-9002(92)90858-2
30. M. Mazouz, L. Ghedira, E. Voutier, Determination of shower central position in laterally segmented lead-fluoride electromagnetic calorimeters. J. Instrum. **11**, P07001 (2016). doi:10.1088/1748-0221/11/07/P07001